



## Clogging transition of granular flow in porous structures

Wenchao Fang,<sup>1</sup> Sheng Chen <sup>1,\*</sup> Shuiqing Li,<sup>2</sup> and Iker Zuriguel <sup>3</sup>

<sup>1</sup>State Key Laboratory of Coal Combustion, School of Energy and Power Engineering, Huazhong University of Science and Technology, Wuhan 430074, China

<sup>2</sup>Key Laboratory for Thermal Science and Power Engineering of Ministry of Education, Department of Energy and Power Engineering, Tsinghua University, Beijing 100084, China

<sup>3</sup>Departamento de Física, Facultad de Ciencias, Universidad de Navarra, E-31080 Pamplona, Spain



(Received 30 August 2023; accepted 13 June 2024; published 10 July 2024)

The clogging transition of granular flow through a disordered porous structure is investigated by three-dimensional discrete element simulations. Results reveal the existence of an intermittent flow state, which has been already observed for active particles or agitated grains, but is absent in single-pore flows of passive particles. Interestingly, the analysis of the intermittent dynamics shows similar attributes to the bottleneck flow of active grains, i.e., exponential distribution of flowing intervals and power-law tails for the clogging times. Precisely, based on the exponent of the power-law tail, a clogging phase diagram for porous structures is proposed in the plane of the scaled pore size  $D/d_p$  and the friction coefficient  $\mu_s$ . Then, we demonstrate that the intermittency arises from a delay in the dissipation of particles' kinetic energy after clogging imposed by the porous structure. Finally, the maximum achievable particle flow rate driven by gravity is predicted from the Froude number  $Fr_m$ , which linearly scales with the pore size and the friction coefficient.

DOI: [10.1103/PhysRevResearch.6.033046](https://doi.org/10.1103/PhysRevResearch.6.033046)

### I. INTRODUCTION

A group of discrete bodies passing through a narrowing often experiences clogging, which halts the flow. This phenomenon has been observed in various systems, including the discharge of grains from a silo [1–4], aerosol filtration [5,6], wastewater treatment [7], and pedestrian room evacuation [8,9]. For simplicity, extensive research has focused on the clogging transition for granular passing through a single outlet. In this system, a critical outlet size exists delimitating clogging and no-clogging regions [10–12]. The clogging process occurs when a group of particles coincides above the outlet in a stable configuration (an arch) [13,14] and resists until the kinetic energy of the system is dissipated. When this occurs, the system remains clogged unless an external vibration is applied to break the arch. It is precisely in this vibrated scenario where flow intermittency emerges characterized by alternating periods of clogging and flowing. Statistically, the duration of flowing intervals displays an exponential distribution, implying a constant probability of clog formation [15]. Distinctly, the duration of temporary clogs displays a power-law tail,  $p(\tau) \sim \tau^{-a}$ . The system is considered clogged when the exponent  $a$  is smaller than 2 and the average clog duration  $\langle \tau \rangle$  diverges [15–17]. Based on this feature, a qualitative representation of the clogging state diagram for single-outlet

flow has been proposed, grouping all relevant variables into three generic parameters [15].

Compared to granular flow through a single outlet, little is known about the flow-clogging transition in porous structures, a system that is gaining increasing attention because of its related applications. For instance, metallic porous blocks have been employed in particle solar receivers to regulate particles' residence time and enhance heat transfer [18–20]. However, an improper choice of porous size can lead to clogging of granular flow, a phenomenon also observed in subsurface-flow wetlands [7]. Unfortunately, despite the importance of these applications, the mechanisms that determine the transition between continuous flow and clogged states, as well as the maximum achievable flow rate, have not been thoroughly investigated. Indeed, although there are some recent related works on the flow of particles in 2D obstacle arrays [21–27], significant distinctions in problem dimensionality and particle driving mechanisms point out the necessity of further investigating the flow of discrete systems in disordered porous structures.

### II. EMERGENCE OF INTERMITTENT FLOW STATE

In this study, we implement numerical simulations using a three-dimensional discrete element method. The porous structure [Fig. 1(a)] is constructed using Voronoi tessellation [28] (see Appendix A for details) in a domain with dimensions  $L_x \times L_y \times L_z$  of 6 mm  $\times$  3 mm  $\times$  20 mm. The selection of these values stems from moving-bed particle heat exchangers [29,30] but larger porous structures have also been investigated (see Appendix C). Note that similar confined particle flows are also encountered in diverse industrial scenarios [31–33]. The pore size is characterized by  $D$ , the diameter of

\*Contact author: sheng\_chen@hust.edu.cn

Published by the American Physical Society under the terms of the Creative Commons Attribution 4.0 International license. Further distribution of this work must maintain attribution to the author(s) and the published article's title, journal citation, and DOI.

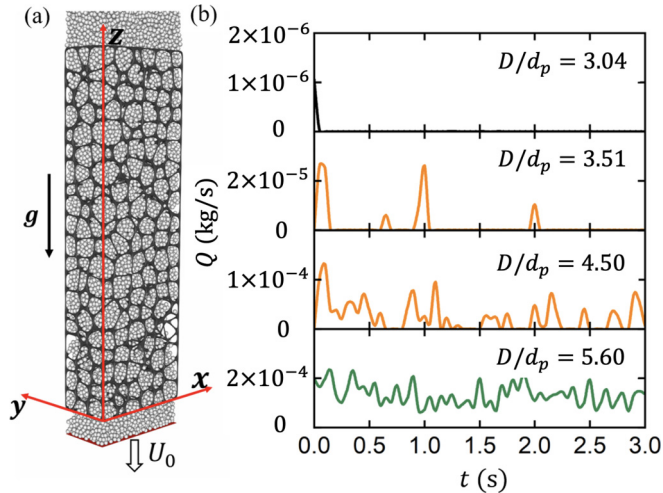


FIG. 1. (a) Simulation setup of granular flow in a porous structure. (b) The temporal evolution of the particle mass flow rate at the bottom of the porous structure  $Q$  for four scaled pore sizes  $D/d_p$  as indicated in each panel.

a sphere with a volume equivalent to the average pore volume. All the porous structures in the simulation have a minimum of three pores in all directions, ensuring that the minimum image convention was not violated. It is worth noting that the porous frame lacks periodicity in the  $y$  direction. However, additional simulations, which utilize a periodic structure generated from a Voronoi lattice and periodic images, demonstrate that this mismatch has a negligible effect on the flow (see Appendix C).

At the bottom ( $z = 0$ ) of the porous structure there is a flat plate, two sidewalls are set at  $x = 0$  and  $L_x$ , and periodic boundary conditions are implemented in the  $y$  direction. The combination of wall and periodic boundary condition is commonly employed in systems that possess a finite dimension in the wall-normal direction and a significantly larger dimension in another direction [34–36]. The particles used are monodisperse spheres with a diameter  $d_p$  that interact via contacts including four terms: an elastic normal force  $F_{NE,ij} = \frac{4}{3}E\sqrt{R}\delta_n^{\frac{3}{2}}$ , a damping normal force  $F_{ND,ij} = \eta_N \mathbf{v}_{ij} \cdot \mathbf{n}_{ij}$ , a sliding friction  $F_{S,ij} = \min[k_T \delta_T + \eta_T \mathbf{v}_{ij} \cdot \boldsymbol{\xi}_S, \mu_s (F_{NE,ij} + F_{ND,ij})]$ , and a rolling torque  $M_{R,ij} = -\mu_r (F_{NE,ij} + F_{ND,ij}) R \boldsymbol{\xi}_R$ . Here,  $E$  is the equivalent Young's modulus,  $R$  the reduced radius,  $\delta_n$  the deformation of particles in the normal direction,  $\delta_t$  the relative tangential displacement.  $\eta_N$  and  $\eta_T$  are the damping coefficients, which are related to the coefficient of restitution ( $e = 0.6$  although results for other values are presented in Appendix D).  $\mu_s$  and  $\mu_r$  are the sliding and rolling friction coefficients. Details on the simulation are given in Appendix B.

The same contact models are adopted to describe the interaction between the porous structure (or the plate) and particles by introducing the effective radius of the contact surface. An important parameter in the interaction is the particle-particle friction coefficient  $\mu_s$ , so its effect on the dynamics will be explored here together with the scaled pore size  $D/d_p$ .

The simulations begin by randomly adding particles above the bottom plate until reaching a bed height  $h$  satisfying  $h \gg L_z$ . This ensures that the particle motion in the porous

media is independent of the packing height [37,38]. After the packing reaches a mechanically stable state, the bottom plate is moved along the  $-z$  direction with a constant velocity  $U_0$ . Depending on the magnitude of  $U_0$ , there are two possible scenarios. (1) For slow plate velocities, the grain motion is constrained by the plate so it strongly depends on  $U_0$ ; (2) with a sufficiently large  $U_0$ , the granular flow reaches its maximum achievable flow rate under the influence of gravity, in a scenario analogous to removing the piston or opening a gate at the bottom.

We start focusing on this second scenario and computing the particle mass flow rate exiting the porous structure  $Q$ . The temporal evolution of  $Q$  is depicted in Fig. 1(b) for four distinct scaled pore sizes  $D/d_p$ . For  $D/d_p = 3.04$ , the flow rate remains essentially zero after an initial release of a few particles, representing a clogged state. As  $D/d_p$  increases to 3.51, an intermittent flow regime emerges, characterized by alternating flowing and arrested intervals. When  $D/d_p$  increases to 4.50 flowing intervals become more frequent, and then a transition to a continuous flow state occurs for  $D/d_p = 5.60$ . Remarkably, the transition from clogged to flowing state through a region of intermittent flow is normally observed when particles are active [15] or, for passive particles, if there is an external perturbation [16,39,40]. The reason is that intermittency only appears when arches are formed and destroyed, a process for which a source of energy (either internal or external) is necessary. Here, we show that an intermittent flow state for passive particles can be induced by the porous structure without applying external perturbations, highlighting the unique features introduced by this geometry.

### III. A CLOGGING PHASE DIAGRAM FOR POROUS STRUCTURE

We then analyze the properties of the intermittent flow looking at (i) the avalanche size  $s$ , defined as the number of particles released from the outlet during a flowing interval, and (ii) the clogging lifetime  $\tau$ , which is the duration of a blockage. As shown in Fig. 2(a), the distributions of normalized avalanche size  $s/\langle s \rangle$  are exponential for all  $D/d_p$  values explored. For cases with  $D/d_p \leq 4.25$ , the data points locate around the line with a slope of  $-1$ , as reported for single-pore flows [15]. When  $D/d_p$  increases to 4.5, the granular flow enters the semicontinuous regime and burst events with a particularly large  $s$  are observed. This leads to a second peak at  $s/\langle s \rangle \approx 3.5$  on the curve of  $D/d_p = 4.5$  and a faster decrease of  $n(s/\langle s \rangle)$  (with a slope  $-1.73$ ) at small  $s/\langle s \rangle$  values. The average avalanche size  $\langle s \rangle$  is displayed in the inset of Fig. 2(a) evidencing that, as  $D/d_p$  increases, the system approaches the continuous flow state and the average avalanche size  $\langle s \rangle$  diverges.

In Fig. 2(b), the complementary cumulative distribution function (CCDF),  $P(T > \tau)$ , of the clogging lifetime  $\tau$  is represented for different pore sizes (note that for  $D/d_p > 4.5$  there are no distributions represented as the flow becomes continuous). In all cases, the CCDF is heavy-tailed and can be fitted to a power law  $P(T > \tau) \sim \tau^{-\alpha}$ . Clearly, as the pore size reduces, the decay of  $P(T > \tau)$  becomes slower indicating that the blockages last for a longer period. The exponent  $\alpha$  can be related to the exponent of the probability density

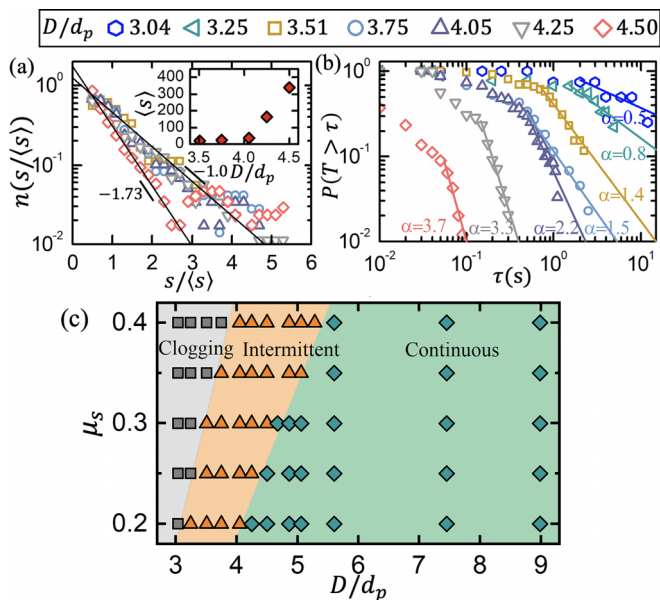


FIG. 2. (a) Probability density function of the scaled avalanche size  $s/\langle s \rangle$  in semilogarithmic scale. The friction coefficient is fixed at  $\mu_s = 0.3$  and different pore sizes  $D/d_p$  are implemented as indicated in the legend. The two dashed lines are guides to the eye with slopes of  $-1$  and  $-1.73$ , respectively. Inset: Average avalanche size  $\langle s \rangle$  as a function of the pore size. (b) CCDF of the clogging lifetime  $\tau$  for the same experiments as in (a). Lines represent power-law fittings with  $\tau^{-\alpha}$ . (c) Clogging diagram in the plane of relative pore size  $D/d_p$  and friction coefficient  $\mu_s$ . The gray squares represent the clogged state, the orange triangles the intermittent flow, and the green diamonds the continuous flow.

function of the clogging lifetime  $[p(\tau)]$  by  $\alpha = a - 1$ . Therefore, when the exponent  $\alpha \leq 1$  (or  $a \leq 2$ ), the mean clogging lifetime  $\langle \tau \rangle = \int_0^\infty \tau \times p(\tau) d\tau$  diverges, and the granular flow is said to be in a clogged state [15,17]. On the contrary, if  $\alpha > 1$ , the flow remains intermittent and no permanent clogging occurs. As the pore size decreases and the system approaches the clogging threshold, the statistics are constrained by the limited occurrence of clogging events. This limitation arises from the prolonged duration of individual clogging events and the associated high computational cost. Consequently, there is an inherent uncertainty associated with the fitted value of the exponent. Nonetheless, this uncertainty does not significantly impact the key findings presented in this study because the exponent  $\alpha$  consistently decreases as  $D/d_p$  decreases.

After conducting extensive simulations, a clogging phase diagram is depicted in the plane of the scaled pore size  $D/d_p$  and friction coefficient  $\mu_s$  [Fig. 2(c)]. As the friction coefficient increases and the pore size decreases, the system transits from continuous to intermittent, and then to clogged states. When comparing with the single bottleneck case, where an abrupt transition occurs from continuous flow to clogged in the region of  $D/d_p$  going from 5 to 8 [12,41], two main features of the flow in porous structures should be explained: (1) once a clog is formed, it may be shattered leading to intermittent flow; (2) formation of clogs is more difficult as the transition from continuous to intermittent occurs in the region of  $D/d_p$  going from 4 to 5.25.

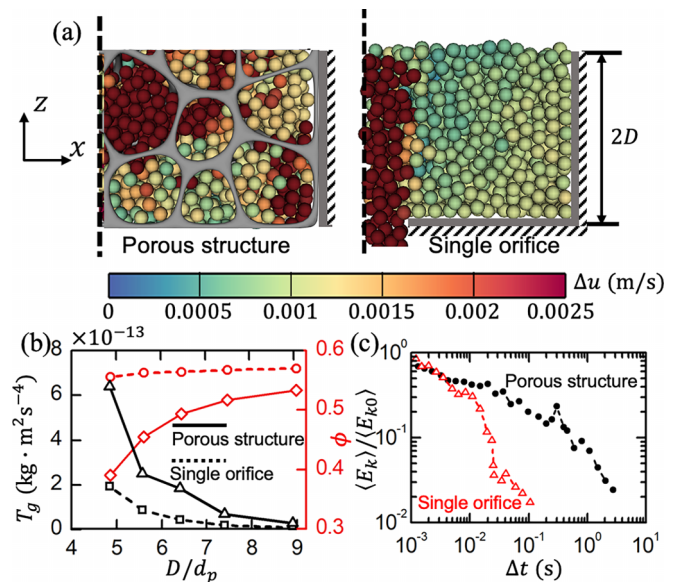


FIG. 3. (a) Granular flow at the bottom of the porous structure (left) and in a single-pore system (right). The walls are indicated by gray lines and the vertical black dashed line signals the centerline of the system. Particles are colored according to the velocity fluctuation  $\Delta u$ . Here,  $D/d_p = 5.6$  and  $\mu_s = 0.3$ . (b) Granular temperature  $T_g$  and the packing fraction  $\phi$  in the near-outlet region as a function of the scaled pore size  $D/d_p$ . (c) Evolution of the particle's mean kinetic energy  $\langle E_k \rangle$  after a blockage event for porous flow with  $D/d_p = 3.25$  and a single orifice with  $D/d_p = 4.05$ . Different  $D/d_p$  values are adopted to achieve a similar extent of blockage. Here,  $\langle E_{k0} \rangle$  is the particle mean kinetic energy at the moment of blockage (at  $\Delta t = 0$ ).

The reduced susceptibility to clogging in porous structures can be attributed to random collisions between particles and the porous structure, which leads to frequent changes in particle velocity and intensifies the randomness of particle motion. In addition, the porous structure can create void space above the bottlenecks, thereby reducing the pressure that particles experience in the downstream direction, a behavior similar to the one observed when suitably placing an obstacle above the bottleneck in a silo [42,43]. To test this idea, we measure the volume fraction ( $\phi$ ) and the velocity fluctuation ( $\Delta u$ ) at the bottom of the system for both the porous structure and the single bottleneck [see Fig. 3(a)]. Here,  $\Delta u$  is calculated as  $\Delta u = \sqrt{(v_x - \bar{v}_x)^2 + (v_y - \bar{v}_y)^2 + (v_z - \bar{v}_z)^2}$ , with  $\bar{v}_x$  representing the spatial average velocity in the  $x$  direction in the near-outlet region. The near-outlet region here is defined as the area within  $2D$  above the outlet, and only the right half of the system is considered due to its symmetry. We observe greater velocity fluctuations in the porous structure compared to the single pore. Additionally, the distribution of velocity fluctuations is relatively uniform in the porous structure, whereas large  $\Delta u$  values only appear above the bottleneck in the single-pore case. In Fig. 3(b), we plot the granular temperature  $T_g$ , defined as  $T_g \equiv (m/3)\langle (v_x - \langle v_x \rangle)^2 + (v_y - \langle v_y \rangle)^2 + (v_z - \langle v_z \rangle)^2 \rangle$  [44–46] with  $\langle v_x \rangle$  being the temporal and spatial average velocity, and the particle volume fraction  $\phi$  in the near-outlet region for different  $D/d_p$ . Remarkably, the porous structure leads to higher granular temperatures and lower volume fractions than the single pore, hence preventing

arch formation. The differences, which are rather important when  $D/d_p$  is small, become significantly reduced as  $D/d_p$  increases and the flow becomes continuous.

On the origin of the intermittency, we have discovered that the porous structure prevents the quick dissipation of the energy observed in single bottlenecks right after an arch obstructs the outlet. This phenomenon is illustrated in Fig. 3(c), which presents the evolution of the mean value of the particle's kinetic energy  $\langle E_k \rangle$  when a blockage event occurs (at  $\Delta t = 0$ ) for both single-pore flow and porous granular flow. In the single-pore flow, the kinetic energy decreases by two orders of magnitude in approximately 0.1 s, whereas in the porous structure the process takes much longer ( $\approx 3$  s). Despite the bottom part of the porous system being blocked, the flow remains nonarrested in other regions due to the geometrical hindrance for the flow in the vertical direction imposed by the porous structure and the low associated volume fractions. Therefore, particles with finite kinetic energy can impact the arches formed at the bottom and shatter them, hence resuming the flow. This argument is further supported by the fact that particles with lower values of  $e$  are more susceptible to clog (see Appendix D). Overall, the findings reported in Fig. 3 elucidate how the interaction between particles and the porous structure reduces the occurrence of clogging and provides insight into the mechanism underlying the apparition of the intermittent state in passive granular flows through porous media.

#### IV. MAXIMUM FLOW RATE

Finally, we focus on the continuous flow state, for which the mass flow rate and its maximum achievable value are the most important parameters. Here, we measure the flow rate,  $Q$ , while varying the bottom plate velocity,  $U_0$ . Figure 4(a) shows that, for all pore sizes,  $Q$  initially increases linearly with  $U_0$  until a value  $U_{0,\max}$ , where the flow rate reaches its maximum value  $Q_m$  and remains constant afterward. Interestingly,  $D/d_p$  does not affect the linear growth rates of  $Q$  but strongly determines the transition plate velocity,  $U_{0,\max}$ , and therefore, the maximum flow rate,  $Q_m$ . The flow rate  $Q$  can be described by

$$Q = \begin{cases} 0.0207 \times U_0, & U_0 < U_{0,\max}, \\ Q_m, & U_0 \geq U_{0,\max}, \end{cases} \quad (1)$$

where, as expected, the coefficient 0.0207 approximately equals  $L_x L_y \rho_p \phi$ , with  $\rho_p = 2000 \text{ kg/m}^3$  and  $\phi = 0.575$  being the particle density and the volume fraction of particles in the bed, respectively. The goodness of this expression is proved by the nice collapse of all the data after normalization, i.e., representing  $Q/Q_m$  versus  $U_0/U_{0,\max}$  as in the inset of Fig. 4(a).

Next, to predict the maximum mass flow rate  $Q_m$ , we group the parameters that affect it into three dimensionless numbers: the Froude number  $Fr_m \equiv Q_m / (S_p \rho_p g^{0.5} d_p^{0.5})$ , where  $S_p = L_x L_y$  is the area of the bottom plane; the size ratio  $D/d_p$ ; and the friction coefficient  $\mu_s$ . The dependence of  $Fr_m$  on  $D/d_p$  is reported in Fig. 4(b) for three friction coefficients. When  $D/d_p$  is small,  $Fr_m \approx 0$ , indicating a clogged state. As  $D/d_p$  increases,  $Fr_m$  undergoes a nonlinear growth (approximately in the region of intermittent flow) and then increases linearly

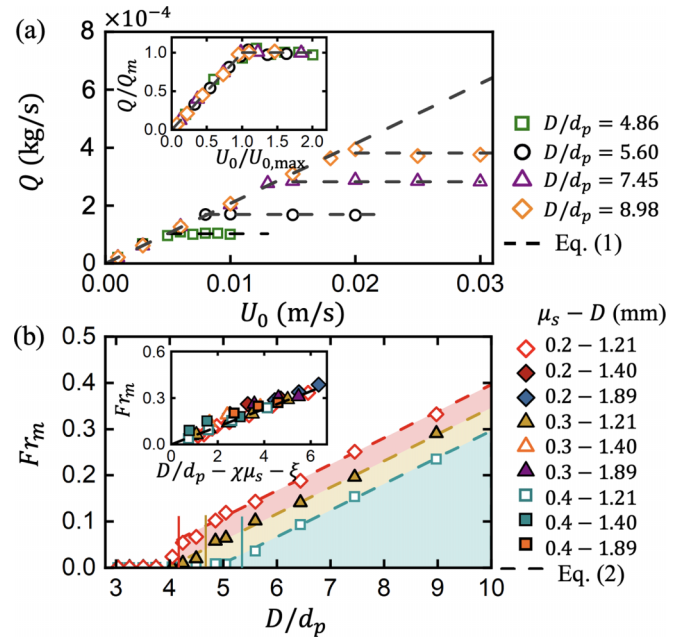


FIG. 4. (a) Mass flow rate  $Q$  as a function of the bottom plate velocity  $U_0$  for  $\mu_s = 0.3$  and different values of  $D/d_p$ . The inset is the dimensionless flow rate  $Q/Q_m$  versus dimensionless bottom plate velocity  $U_0/U_{0,\max}$ . Here,  $Q_m$  and  $U_{0,\max}$  are, respectively, the maximum flow rate and maximum bottom plate velocity when the  $U_0$  curve enters the plateau. (b) Dimensionless maximum flow rate  $Fr_m$  as a function of  $D/d_p$  for particles with different friction coefficients  $\mu_s = 0.2, 0.3$ , and  $0.4$ . The vertical lines separate the intermittent and continuous flow states. The dashed lines are fitting results using Eq. (2). Inset:  $Fr_m$  versus  $D/d_p - \chi\mu_s - \xi$ .

with  $D/d_p$  as the flow becomes continuous (right side of the vertical lines). The results in Fig. 4(b) are then fitted according to

$$Fr_m = \Theta(D/d_p - \chi\mu_s - \xi), \quad (2)$$

where the fitting constants  $\Theta$ ,  $\chi$ , and  $\xi$  are 0.057, 8.72, and 1.35, respectively. Note that this formula applies only to the continuous flow state (controlled by gravity with  $Fr_m < 1$ ) and no longer holds when the particle flow is intermittent. To verify the effectiveness of Eq. (2), in the inset of Fig. 4(b) we represent  $Fr_m$  versus  $D/d_p - \chi\mu_s - \xi$  for different friction coefficients and pore sizes. Using the same values of the fitting constants, all data points collapse on top of the curve of Eq. (2), indicating that the ability of particles to flow through a porous medium under the action of gravity is mostly determined by the gravity itself, the size ratio, and the friction coefficient. The effect of other parameters, including the coefficient of restitution and thickness of the porous structure backbone, on the dimensionless maximum bed flow rate was also investigated (see Appendixes C and D). The dimensionless maximum flow rate is not strongly affected when the mean cross-sectional area of the backbone increases from  $S = 0.0104 \text{ mm}^2$  to  $S = 0.0164 \text{ mm}^2$ . In contrast, the coefficient of restitution has a non-negligible effect on the flow rate. Specifically, particles with higher values of  $e$ , indicating lower energy dissipation during collisions, demonstrate

an enhanced maximum flow rate, given fixed values of  $D/d_p$  and  $\mu_s$ .

## V. CONCLUSIONS

In summary, we have performed simulations of granular flow through disordered porous structures. We discover that, for a range of pore sizes, this geometry leads to the emergence of intermittent flow without vibration or any other kind of external input of energy. The physical mechanism behind this intermittency is the temporal decorrelation between outlet blockage and energy dissipation inside the porous media. Moreover, as in the case of active particles passing through a single pore, the power-law tail distribution for clogging times allows distinguishing between the clogged and the intermittent flow states. From this, a clogging phase diagram is constructed in the plane of the scaled pore size  $D/d_p$  and friction coefficient  $\mu_s$ , revealing that the porous structure also prevents clog formation compared with the single bottleneck. This phenomenon is justified by the higher granular temperature and lower particle volume fraction developed in the porous structure. Finally, the maximum reachable flow rate in the continuous flow regime is predicted from the Froude number  $Fr_m$ , which is expressed as a linear function of the scaled pore size  $D/d_p$  and the friction coefficient  $\mu_s$ .

The current work presents an attempt to forecast the clogging transition of granular flow within porous structures confined in a narrow channel. Preliminary findings demonstrate that enlarging the size of the porous media induces a shift of the transitions toward smaller values of  $D/d_p$ . So, questioning how the dynamics would be in a hypothetical system of infinite size seems like an obvious extension of this work. In the same way, further extensive research is required to elucidate the impact of walls, analyze correlations in particle movement, and investigate the segregation/mixing behavior of binary samples.

## ACKNOWLEDGMENTS

S.C. acknowledges support from the National Natural Science Foundation of China (Grant No. 52376144). I.Z. acknowledges funding by the Spanish Government, through Grant No. PID2020-114839GB-I00 supported by MCIN/AEI/10.13039/501100011033.

## APPENDIX A: CONSTRUCTION OF THE POROUS STRUCTURE

To construct a porous media, various techniques are available, such as the cell unit method [47,48], the implicit surfaces method [49,50], the packing of spheres, and the Voronoi tessellation method. Among these, we have chosen Voronoi tessellation as it presents several notable advantages, such as simplicity of the process, controllable pore shapes, and close resemblance to actual metal foams. Indeed, this technique has been previously implemented in experiments to construct porous structures in which several parameters, including porous irregularity, have been modified [28,51].

The generation process is as follows: First, a cuboid region with dimensions of  $L_x \times L_y \times L_z = 6 \text{ mm} \times 3 \text{ mm} \times 20 \text{ mm}$  was created, which represents the space occupied by the

porous structure. Next, an ordered cube lattice containing  $n$  layers along the  $z$  direction was generated within this region. The coordinates of the lattice points were denoted as  $\mathbf{P}_i = (x_i, y_i, z_i)$ , where the distances between adjacent points in the  $x$  and  $y$  directions were  $b$  and  $c$ , respectively, and the distance between adjacent layers was denoted as  $a$ . Subsequently, a spherical region with a radius of  $R_m$ , termed a probability sphere, was generated centered at each lattice point  $\mathbf{P}_i$ . Within each probability sphere, a new point  $\mathbf{P}'_i = (x'_i, y'_i, z'_i)$  was randomly generated to replace the original point  $\mathbf{P}_i$ , giving rise to a series of irregular lattices. The relationship between points  $\mathbf{P}_i$  and  $\mathbf{P}'_i$  is as follows:

$$\begin{aligned} x'_i &= x + R_m \times (2 \times \mathcal{R} - 1), \\ y'_i &= y + R_m \times (2 \times \mathcal{R} - 1), \\ z'_i &= z + R_m \times (2 \times \mathcal{R} - 1). \end{aligned} \quad (\text{A1})$$

Here,  $R_m$  is the radius of the probability sphere, which is set as  $R_m = \min[a/3, b/3, c/3]$  in this work, and  $\mathcal{R}$  is a random number uniformly distributed within the range  $[0, 1]$ .

Voronoi cells are generated around irregular lattice points  $\mathbf{P}'_i$ , also known as seed points. Each Voronoi cell represents the region of space that is closest to a particular seed point in comparison to the other seed points. The neighboring points associated with each seed point are identified, and subsequently, edges are constructed that bisect the line segments connecting the seed point to its neighboring points. These edges act as the boundaries of the corresponding Voronoi cell. By connecting the Voronoi edges, closed polyhedra are formed, enclosing the regions surrounding each seed point. In cases where a seed point is close to the simulation domain boundaries, these edges are modified to align with the shape of the boundary. This process partitions the space into distinct cells, as depicted in Fig. 5(a) (shown in a two-dimensional representation, although the actual implementation is in three dimensions).

The intersections of Voronoi edges are then selected as the centerlines for the porous structure. Around these centerlines, cylinders are generated with an average cross-sectional area of  $S = 0.0104 \text{ mm}^2$ . The average effective diameter (thickness) of the cylinder corresponds to 0.115 mm. To mimic the characteristics observed in actual foam metal structures [18], the cylinders have a smaller cross-sectional area in the middle (referred to as  $S_{\min}$ ) and larger cross-sectional areas at the ends (referred to as  $S_{\max}$ ), with a ratio of  $S_{\min}/S_{\max} \approx 0.6$ . Together, these cylinders constitute the backbone of the porous structure [Fig. 5(b)]. Note that, in the numerical implementation, the curved surfaces are subsequently discretized using a dense grid of points. Each grid point stores coordinates and local curvature information, which is utilized when calculating the contact forces within the framework of the discrete element method (DEM).

The dimension and shape of cells in the porous structure can be adjusted by varying the number of seed points and the value of parameters  $a$ ,  $b$ , and  $c$ , which ranged from 1 mm to 1.5 mm. In the main text, the majority of the numerical cases feature a fixed size for the porous medium of  $6 \text{ mm} \times 3 \text{ mm} \times 20 \text{ mm}$  including  $N_p = 360$  cells. There are, however, some exceptions to this in the results of Fig. 6 in Appendix C where the porous frame is enlarged (see

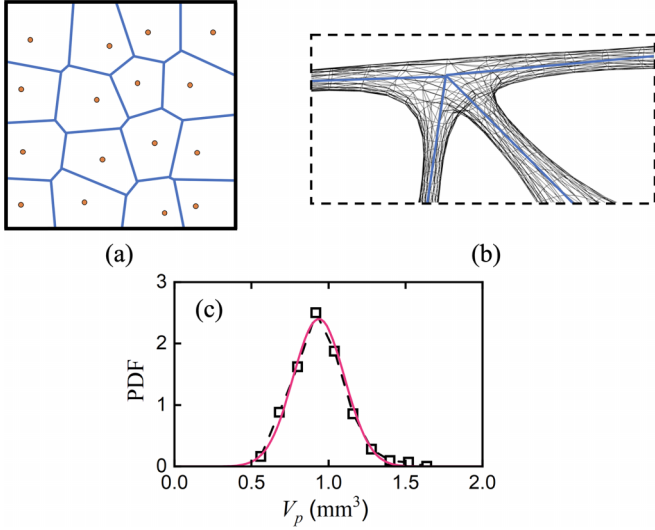


FIG. 5. (a) Illustration of Voronoi tessellation in two-dimensional form. The solid black line stands for the edges. (b) Detail of the backbone of the porous structure. The intersections of Voronoi edges (black lines) and cylinders are generated around the centerlines, which have been discretized using a dense grid of points. (c) Probability density function of the volume of each cell in the porous structure  $V_p$ . The solid red line depicts a normal distribution.

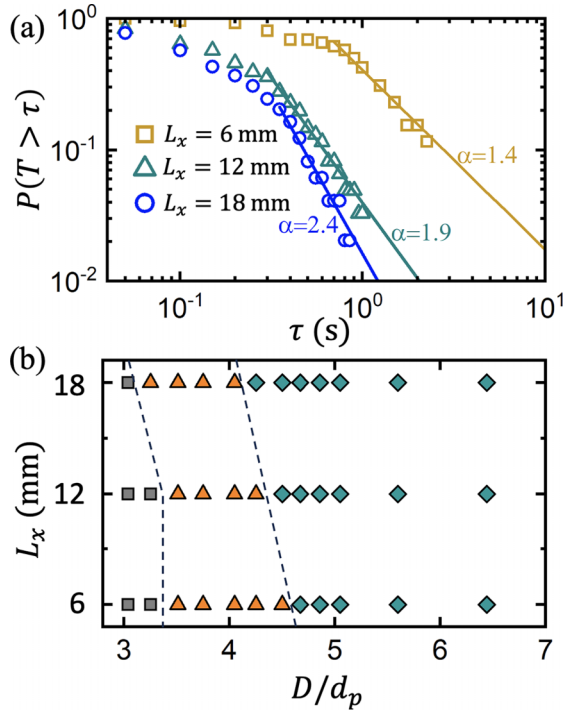


FIG. 6. (a) CCDF of the clogging lifetime  $\tau$  for  $L_x = 6$  mm, 12 mm, and 18 mm with a fixed aspect ratio  $L_x/L_y = 2$  of the cross section. Here,  $D/d_p = 3.51$  and  $\mu_s = 0.3$ . Lines represent power-law fittings with  $\tau^{-\alpha}$ . (b) Clogging diagram in the plane of the scaled pore size  $D/d_p$  and system size  $L_x$ .

TABLE I. Parameters of particle properties in the DEM simulation.

Parameter	Symbol	Value	Unit
Particle diameter	$d_p$	0.135 ~ 0.4	mm
Particle density	$\rho_p$	2000	kg/m <sup>3</sup>
Young's modulus of particles	$E_i$	10 <sup>7</sup>	Pa
Poisson ratio of particle	$\nu_i$	0.3	
Coefficient of sliding friction	$\mu_s$	0.2 ~ 0.4	
Coefficient of rolling friction	$\mu_r$	0.3	
Coefficient of restitution	$e$	0.3, 0.6, 0.9	

Table II). By employing Monte Carlo methods, one can obtain the volume  $V_p$  of each cell (excluding the volume of the backbone). The probability density function of  $V_p$  is illustrated in Fig. 5(c), which is close to a normal distribution (depicted by the solid red line). The average pore volume  $\langle V_p \rangle$  is 0.937 mm<sup>3</sup>. The average equivalent pore diameter,  $D$ , defined as the diameter of a sphere with the same volume as the average pore volume, is calculated through

$$D = \left( \frac{6\langle V_p \rangle}{\pi} \right)^{(1/3)} = \left[ \frac{6 \times (V - V_F)}{\pi \times N_D} \right]^{(1/3)}, \quad (\text{A2})$$

where  $V$  represents the volume of space occupied by the porous structure ( $V = L_x \times L_y \times L_z$ ),  $V_F$  is the volume of the porous frame, and  $N_D$  is the number of pores within the porous structure.

In this study, our primary focus is to investigate the impact of the scaled pore size  $D/d_p$  on the flow behavior of granular particles within a porous structure. To achieve this, several variables are kept constant: the average equivalent pore diameter  $D$ , the dimensions of the porous structure ( $L_x$ ,  $L_y$ , and  $L_z$ ), and the thickness of the skeleton. Meanwhile, we vary the particle size  $d_p$  to obtain different values of  $D/d_p$ . However, as said before, in Fig. 4(b) of the main text, we modify the value of  $D$  while keeping  $L_x/D$  constant, to validate the universality of the scaling for the maximum bed flow rate  $Q_m$ . Also in Appendix C, the effect of changing several parameters is investigated.

## APPENDIX B: DISCRETE ELEMENT METHOD

In the discrete element method, the motion of every particle is simulated following Newton's laws. Moreover, the interactions between contact particles or between particles and the porous structure are modeled based on soft-sphere contact models. The linear and angular momentum equations of particles are expressed as

$$m_i \frac{d\mathbf{v}_i}{dt} = \mathbf{F}_{C,i} + \mathbf{F}_{g,i}, \quad (\text{B1a})$$

$$I_i \frac{d\boldsymbol{\omega}_i}{dt} = \mathbf{M}_{C,i}, \quad (\text{B1b})$$

where  $m_i$  and  $I_i$  are the mass and the moment of inertia of particle  $i$ ,  $\mathbf{v}_i$  and  $\boldsymbol{\omega}_i$  are the translational and angular velocities of the particle,  $\mathbf{F}_{C,i}$  and  $\mathbf{M}_{C,i}$  are the contact force and torque acting on particle  $i$  from other particles or walls that are in contact with particle  $i$ , and  $\mathbf{F}_{g,i}$  is the gravitational force acting on particle  $i$ .

TABLE II. Simulation condition for each figure in the main text and Appendixes.

	Equivalent pore diameter, $D$ (mm)	Particle diameter, $d_p$ (mm)	Dimensions of porous structure, $L_x, L_y, L_z$ (mm)	Coefficient of sliding friction, $\mu_s$	Coefficient of restitution, $e$
In main text:					
Fig. 1(b)	1.21	0.217 ~ 0.4	6, 3, 20	0.3	0.6
Figs. 2(a) and 2(b)	1.21	0.135 ~ 0.4	6, 3, 20	0.3	0.6
Fig. 2(c)	1.21	0.135 ~ 0.4	6, 3, 20	0.2 ~ 0.4	0.6
Fig. 3(a)	1.21	0.217	6, 3, 20	0.3	0.6
Fig. 3(b)	1.21	0.135 ~ 0.25	6, 3, 20	0.3	0.6
Fig. 4(a)	1.21	0.135 ~ 0.25	6, 3, 20	0.3	0.6
	1.21	0.135 ~ 0.4	6, 3, 20	0.2, 0.3, 0.4	0.6
Fig. 4(b)	1.40	0.18 ~ 0.25	6.9, 3.45, 23	0.2, 0.3, 0.4	0.6
	1.89	0.2 ~ 0.25	9.2, 4.61, 30.7	0.2, 0.3, 0.4	0.6
In Appendixes:					
Fig. 6(b)	1.21	0.19 ~ 0.4	6, 3, 20	0.3	0.6
	1.21	0.19 ~ 0.4	12, 6, 20	0.3	0.6
	1.21	0.19 ~ 0.4	18, 9, 20	0.3	0.6
Fig. 7	1.21	0.135 ~ 0.35	6, 3, 20	0.3	0.6
Fig. 8	1.21	0.135 ~ 0.4	6, 3, 20	0.3	0.3, 0.6, 0.9

For two touching particles ( $i$  and  $j$ ), we consider the normal elastic force  $F_{NE,ij}$ , the normal damping force  $F_{ND,ij}$ , the sliding friction  $F_{S,ij}$ , and the rolling torque  $M_{R,ij}$  acting on particle  $i$  from particle  $j$ , which are expressed as

$$F_{NE,ij} = \frac{4}{3}E\sqrt{R}\delta_n^{\frac{3}{2}}, \quad (\text{B2a})$$

$$F_{ND,ij} = \eta_N \mathbf{v}_{ij} \cdot \mathbf{n}_{ij}, \quad (\text{B2b})$$

$$F_{S,ij} = \min[k_T \delta_T + \eta_T \mathbf{v}_{ij} \cdot \boldsymbol{\xi}_S, F_{SC,ij}], \quad (\text{B2c})$$

$$M_{R,ij} = -\mu_r F_{N,ij} R \boldsymbol{\xi}_R. \quad (\text{B2d})$$

The elastic normal force  $F_{NE,ij}$  is derived from Hertzian contact theory [52], where  $\delta_n$  is the deformation of particles in the normal direction.  $F_{N,ij} = F_{NE,ij} + F_{ND,ij}$  is the overall normal force. The equivalent Young's modulus  $E$  and the reduced radius  $R$  are given by

$$\frac{1}{E} = \frac{(1 - \nu_i^2)}{E_i} + \frac{(1 - \nu_j^2)}{E_j}, \quad (\text{B3a})$$

$$\frac{1}{R} = \frac{1}{r_{p,i}} + \frac{1}{r_{p,j}}. \quad (\text{B3b})$$

Here,  $E_i$  is the Young's modulus,  $\nu_i$  the Poisson ratio, and  $r_{p,i}$  the radius of particle  $i$ . The damping force is proportional to the normal component of the relative velocity  $\mathbf{v}_{ij} \cdot \mathbf{n}_{ij}$  [53]. Here,  $\mathbf{v}_{ij} = \mathbf{v}_i - \mathbf{v}_j$  is the relative velocity and  $\mathbf{n}_{ij}$  is the unit vector pointing from the centroid of particle  $j$  to the centroid of particle  $i$ . The damping coefficient  $\eta_N$  is given by

$$\eta_N = -2\sqrt{\frac{5}{6}}\beta\sqrt{k_n m^*}, \quad (\text{B4})$$

where  $m^* = (m_i^{-1} + m_j^{-1})^{-1}$  is the equivalent mass,  $\beta$  is the damping factor, which is related to the coefficient of restitution by  $\beta = -\ln e / \sqrt{\ln^2 e + \pi^2}$ , and  $k_n$  is the normal stiffness given by  $k_n = 2E\sqrt{R}\delta_n$ . The friction force  $F_{S,ij}$  is the product of the tangential displacement  $\delta_T = \int_{t_0}^t \mathbf{v}_{ij}(\tau) \cdot \boldsymbol{\xi}_S d\tau$  and the tangential stiffness  $k_T$  [54,55]. Here,  $\boldsymbol{\xi}_S$  is the unit vector in the

tangential direction and  $k_T$  is given by  $k_T = 8G\sqrt{R}\delta_n$ , where  $G$  is the equivalent shear modulus. From the value of  $k_T$ , we obtain the damping coefficient in the tangential direction  $\eta_T$  using an expression analogous to Eq. (B4).

The Coulomb friction limit  $F_{SC,ij}$  is set as the maximum value of the sliding friction, which is expressed as  $F_{SC,ij} = \mu_s F_{N,ij}$  with  $\mu_s$  being the coefficient of the static friction [56]. When the sliding friction  $F_{S,ij}$  reaches the Coulomb limit, the particle will irreversibly slide relative to its neighboring particle.

The rolling friction  $M_{R,ij}$  in Eq. (B2d) is a function of the rolling friction coefficient  $\mu_r$ , the normal force  $F_{N,ij}$ , the distance  $R_r$  between the contact point and the center of mass of particle  $i$ , and the unit angular velocity vector  $\boldsymbol{\xi}_R$  [57]. The parameters in DEM are summarized in Table I. The time step  $\Delta t$  used to solve the equations of motion [Eq. (B1)] is sufficiently small to prevent excessive overlaps between contact particles and to ensure realistic force transmission. The DEM model has been applied to simulate dense granular flow around an immersed cylindrical tube [58] and has been validated by comparing the simulation results with the experimental data from Ref. [59].

As said, the current work focuses on the effect of the scaled particle size  $D/d_p$  and the friction coefficient  $\mu_s$ . The pore size  $D$  is fixed as  $D = 1.21$  mm and the dimension of the porous structure is fixed as  $L_x = 6$  mm,  $L_y = 3$  mm, and  $L_z = 20$  mm for results in Figs. 1(b), 2, 3, and 4(a). Only in Fig. 4(b), the pore size  $D$  was varied while keeping  $D/L_x$  constant to verify the universality of the scaling of the maximum bed flow rate. The values or variation ranges of  $d_p$ ,  $D$ , and  $L$  for each figure are summarized in Table II.

### APPENDIX C: EFFECT OF GEOMETRIC PARAMETERS OF THE POROUS STRUCTURE

The role of the scaled pore size  $D/d_p$  has been discussed in the main text. In this section, the influence of the dimensions

of the porous structure and the thickness of the backbone of the porous frame are investigated.

### 1. Size of the porous structure

The cross-sectional area of the porous structure for all experiments reported in the main text is  $L_x \times L_y = 6 \text{ mm} \times 3 \text{ mm}$ . Here, we present extensive simulations with enlarged cross-sectional areas of  $L_x \times L_y = 12 \text{ mm} \times 6 \text{ mm}$  and  $18 \text{ mm} \times 9 \text{ mm}$ , corresponding to four and nine times the original value, respectively. The coefficient of restitution is  $e = 0.6$  and the coefficient of friction is  $\mu_s = 0.3$ . All the outcomes are condensed in Fig. 6(b), where we present the clogging diagram in the plane of the scaled pore size  $D/d_p$  and system size  $L_x$ . Clearly, when the cross-sectional area increases, the transitions from clogging to intermittent state and from intermittent to continuous state tend to occur at smaller values of  $D/d_p$ . This can be attributed to the fact that achieving a clogged state in the porous structure necessitates the blockage of all pores in the proximity of the outlet. Consequently, enlarging the system size leads to an increased number of pores, making it more challenging for all pores to be simultaneously obstructed. This phenomenon can be quantified by the exponent of the power-law tail in the clogging lifetime distribution [Fig. 6(a)], where an increase in the cross-sectional area results in an increase in the exponent  $\alpha$ , indicating shorter duration of individual blockages. Notably, from Fig. 6(b) we also detect that the width of the intermittent regime on the phase diagram only exhibits a small decrease, if any, as  $L_x$  increases from 6 mm to 18 mm.

### 2. Thickness of the porous structure backbone

The mean cross-sectional area of the backbone is fixed at  $S = 0.0104 \text{ mm}^2$  in the simulations presented in the main text. To preliminarily assess the influence of this parameter, it is increased to  $S = 0.0164 \text{ mm}^2$ , which is approximately 1.6 times its original value. The dimensionless maximum bed flow rate  $Fr_m$  is plotted as a function of the scaled pore size  $D/d_p$  in Fig. 7. One can see that, within the range of  $S$  explored, the flow characteristics (both the dimensionless maximum flow rate and the transition from clogged, intermittent, to continuous states) are not strongly affected.

In the main text simulations, the porous frame lacks periodicity in the  $y$  direction. To examine the potential impact of this mismatch on the flow, additional simulations were conducted using a periodic structure generated from a Voronoi lattice and periodic images. Figure 7 illustrates that the dimensionless maximum flow rate ( $Fr_m$ ) values are essentially identical for granular flows in both periodic and nonperiodic frames.

### APPENDIX D: EFFECT OF COEFFICIENT OF RESTITUTION

According to the results in Fig. 3 of the main text, the porous structure prevents the quick dissipation of the particle's kinetic energy observed in single bottlenecks. Therefore, when arches obstruct the bottom part of the porous structure, particles with finite kinetic energy can impact the arches and shatter them, hence resuming the flow. To further elucidate the role of energy dissipation on the clogging transition of

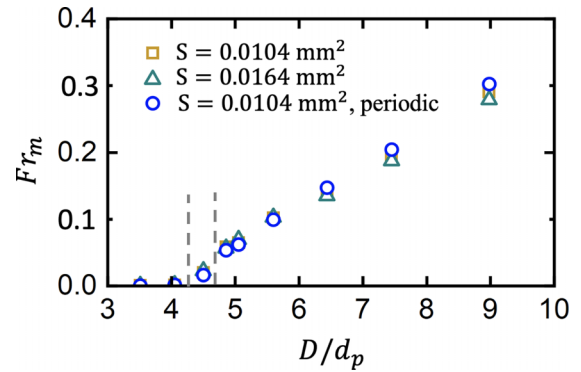


FIG. 7. Dimensionless maximum bed flow rate  $Fr_m$  as a function of the scaled pore size  $D/d_p$  for two different mean cross-sectional areas of the backbone of the porous frame,  $S = 0.0104 \text{ mm}^2$  and  $0.0164 \text{ mm}^2$ . The results for the structure generated from Voronoi lattice and periodic images are also plotted for comparison (circles). The two vertical dashed lines divide the clogging, intermittent, and continuous states. The friction coefficient is fixed at  $\mu_s = 0.3$ .

granular flow in the porous structure, additional simulations using varying values of the coefficient of restitution ( $e$ ), specifically  $e = 0.3, 0.6$ , and  $0.9$ , are conducted. A smaller value of  $e$  indicates a stronger energy dissipation upon collisions.

Figure 8(a) depicts the complementary cumulative distribution function (CCDF),  $P(T > \tau)$ , of the clogging lifetime  $\tau$  for different values of restitution coefficient, while keeping constant pore size ( $D/d_p = 3.51$ ). The tail of the CCDF is fitted to a power law,  $P(T > \tau) \sim \tau^{-\alpha}$ . Notably, the exponent  $\alpha$  displays an increasing trend as  $e$  increases, indicating that particles with lower  $e$  values are more susceptible to clog. This observation aligns with the argument presented in the main text. Furthermore, Fig. 8(b) presents the phase diagram depicted in the plane of  $D/d_p$  and  $e$ . The transition from clogging to an intermittent state, as well as from an intermittent to a continuous state, tends to occur at smaller  $D/d_p$  values when  $e$  increases. These results serve to validate the close relationship between intermittency occurrence and the dissipation of energy during particle-porous structure collisions.

Finally, to investigate the influence of energy dissipation on the maximum flow rate reached in the system, in Fig. 8(c), we present a plot of the dimensionless maximum flow rate ( $Fr_m$ ) as a function of  $D/d_p$  for different  $e$  values. It is observed that particles with a higher restitution coefficient ( $e$ ), indicating lower energy dissipation during collisions, display a greater maximum flow rate for a given  $D/d_p$ . However, as  $D/d_p$  increases, the disparity in  $Fr_m$  diminishes.

In summary, based on the findings in Fig. 8, we can deduce that energy dissipation caused by the viscous damping force influences the transition between clogging, intermittent, and continuous states, but its impact on the flow rate is relatively weak when the pore size is sufficiently large.

### APPENDIX E: VELOCITY PROFILE

In the last part of the main text, we analyze the maximum flow rate at the exit of the bottom structure (bottom plane) and we propose a generic expression in terms of three



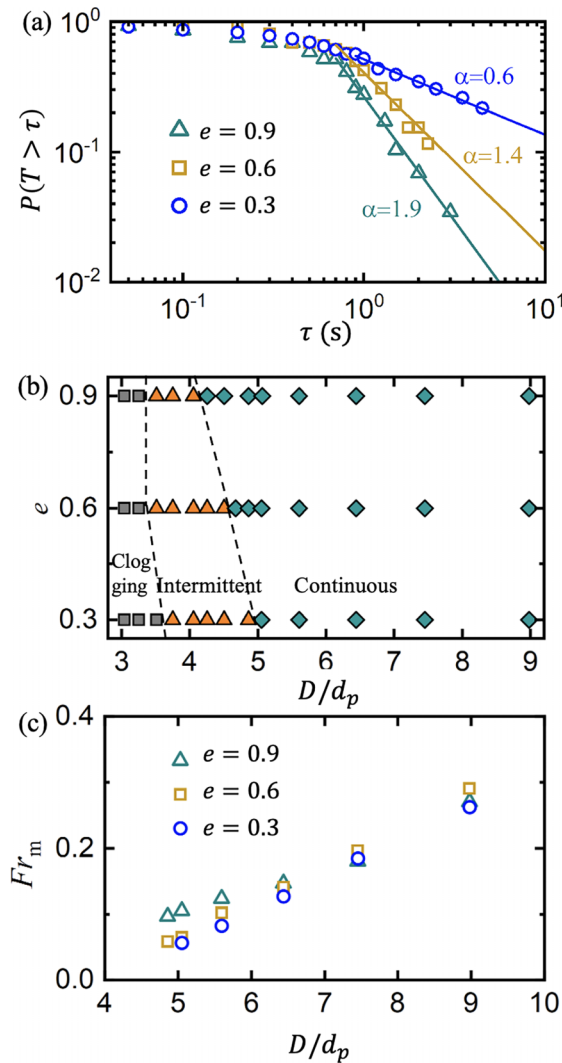


FIG. 8. (a) CCDF of the clogging lifetime  $\tau$  with a fixed pore size  $D/d_p = 3.51$  and coefficient of restitution  $e = 0.3, 0.6,$  and  $0.9$ . Lines represent power-law fittings with  $\tau^{-\alpha}$ . (b) Clogging diagram in the plane of the scaled pore size  $D/d_p$  and coefficient of restitution  $e$ . The gray squares represent the clogged state, the orange triangles the intermittent flow, and the green diamonds the continuous flow. (c) Froude number  $Fr_m$  that is calculated based on the maximum flow rate as a function of  $D/d_p$ .

dimensionless parameters. This analysis will be surely extended in the future looking at the connection of the flow rate with microscopic quantities such as density or velocity that, for the case of single outlets, display important gradients near the orifice. Interestingly, we observe very different behavior for the dynamics in the porous structure. In particular, we

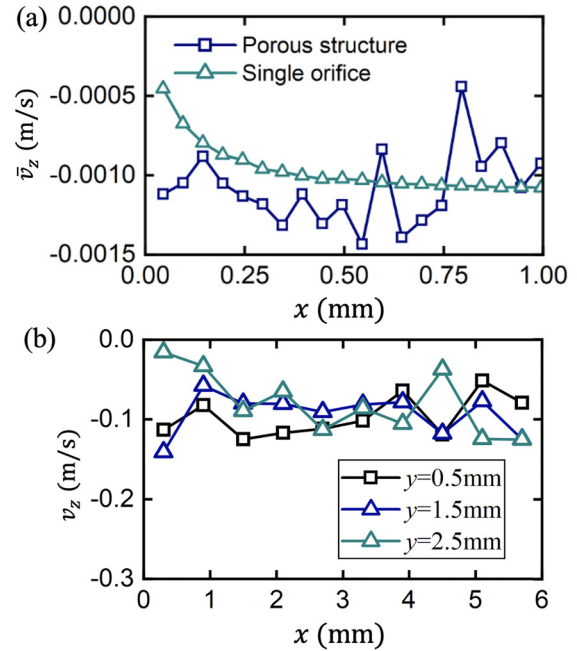


FIG. 9. (a) Mean particle vertical velocity as a function of the distance to the wall in the  $x$  direction ( $x = 0$  corresponds to the wall). The velocity is averaged over particles in vertical slices parallel to the wall with  $0 < y < 3$  mm,  $5$  mm  $< z < 15$  mm, and a thickness of  $0.05$  mm; the scaled pore size is  $D/d_p = 8.98$ . (b) Particle's vertical velocity (averaged over time) measured at the outlet plane of the porous structure. Here, the scaled pore size is  $D/d_p = 5.6$ , the velocity of bottom plane satisfies  $U_0 > U_{0,max}$ , and the coefficient of the sliding friction is  $\mu_s = 0.3$ .

focus on analyzing the velocity profile in two regions: the vicinity of the lateral wall and the bottom of the porous media.

Figure 9(a) displays the velocity profiles in the near lateral wall region for both the porous structure and single-pore flow with a scaled pore size of  $D/d_p = 8.98$ . Notably, in the case of single-pore flow, a low-velocity region induced by wall friction extends approximately  $0.25$  mm. In contrast, no distinct low-velocity region near the wall is observed in porous flow, indicating that the wall effect is limited in porous structure. This behavior can be primarily attributed to the random collisions between particles and the porous framework.

Furthermore, we computed the vertical velocity of particles as they exit the porous media in the case with a pore size of  $D/d_p = 5.6$  and  $U_0 > U_{0,max}$ . The averaged values at different  $x$  and  $y$  coordinates are depicted in Fig. 9(b). Notably, we observe relatively uniform velocity profiles across the outlet plane, which justifies the utilization of the flow rate as a characteristic parameter within the framework of Froude number scaling.

[1] J. Nielsen, Pressures from flowing granular solids in silos, *Philos. Trans. R. Soc. A* **356**, 2667 (1998).  
 [2] I. Zuriguel, L. A. Pugnaloni, A. Garcimartín, and D. Maza, Jamming during the discharge of grains from a silo described as a percolating transition, *Phys. Rev. E* **68**, 030301(R) (2003).

[3] D. Gella, D. Maza, and I. Zuriguel, Granular internal dynamics in a silo discharged with a conveyor belt, *J. Fluid Mech.* **925**, A24 (2021).  
 [4] S. Dunatunga and K. Kamrin, Modelling silo clogging with non-local granular rheology, *J. Fluid Mech.* **940**, A14 (2022).

- [5] D. Thomas, P. Penicot, P. Contal, D. Leclerc, and J. Vendel, Clogging of fibrous filters by solid aerosol particles experimental and modelling study, *Chem. Eng. Sci.* **56**, 3549 (2001).
- [6] S. Chen, W. Liu, and S. Li, Effect of long-range electrostatic repulsion on pore clogging during microfiltration, *Phys. Rev. E* **94**, 063108 (2016).
- [7] P. Knowles, G. Dotro, J. Nivala, and J. García, Clogging in subsurface-flow treatment wetlands: Occurrence and contributing factors, *Ecol. Eng.* **37**, 99 (2011).
- [8] D. Helbing, I. Farkas, and T. Vicsek, Simulating dynamical features of escape panic, *Nature (London)* **407**, 487 (2000).
- [9] D. Helbing, A. Johansson, J. Mathiesen, M. H. Jensen, and A. Hansen, Analytical approach to continuous and intermittent bottleneck flows, *Phys. Rev. Lett.* **97**, 168001 (2006).
- [10] K. To, P.-Y. Lai, and H. K. Pak, Jamming of granular flow in a two-dimensional hopper, *Phys. Rev. Lett.* **86**, 71 (2001).
- [11] K. To and P.-Y. Lai, Jamming pattern in a two-dimensional hopper, *Phys. Rev. E* **66**, 011308 (2002).
- [12] I. Zuriguel, A. Garcimartín, D. Maza, L. A. Pugnaloni, and J. M. Pastor, Jamming during the discharge of granular matter from a silo, *Phys. Rev. E* **71**, 051303 (2005).
- [13] C. Lozano, G. Lumay, I. Zuriguel, R. C. Hidalgo, and A. Garcimartín, Breaking arches with vibrations: The role of defects, *Phys. Rev. Lett.* **109**, 068001 (2012).
- [14] M. E. Cates, J. P. Wittmer, J.-P. Bouchaud, and P. Claudin, Jamming, force chains, and fragile matter, *Phys. Rev. Lett.* **81**, 1841 (1998).
- [15] I. Zuriguel, D. R. Parisi, R. C. Hidalgo, C. Lozano, A. Janda, P. A. Gago, J. P. Peralta, L. M. Ferrer, L. A. Pugnaloni, E. Clément *et al.*, Clogging transition of many-particle systems flowing through bottlenecks, *Sci. Rep.* **4**, 7324 (2014).
- [16] A. Janda, D. Maza, A. Garcimartín, E. Kolb, J. Lanuza, and E. Clément, Unjamming a granular hopper by vibration, *Europhys. Lett.* **87**, 24002 (2009).
- [17] A. Nicolas, Á. Garcimartín, and I. Zuriguel, Trap model for clogging and unclogging in granular hopper flows, *Phys. Rev. Lett.* **120**, 198002 (2018).
- [18] C. Ho, J. Christian, D. Gill, A. Moya, S. Jeter, S. Abdel-Khalik, D. Sadowski, N. Siegel, H. Al-Ansary, L. Amsbeck *et al.*, Technology advancements for next generation falling particle receivers, *Energy Procedia* **49**, 398 (2014).
- [19] A. Calderón, A. Palacios, C. Barreneche, M. Segarra, C. Prieto, A. Rodríguez-Sánchez, and A. I. Fernández, High temperature systems using solid particles as TES and HTF material: A review, *Appl. Energy* **213**, 100 (2018).
- [20] T. Lee, S. Lim, S. Shin, D. L. Sadowski, S. Abdel-Khalik, S. M. Jeter, and H. Al-Ansary, Numerical simulation of particulate flow in interconnected porous media for central particle-heating receiver applications, *Sol. Energy* **113**, 14 (2015).
- [21] H. T. Nguyen, C. Reichhardt, and C. J. O. Reichhardt, Clogging and jamming transitions in periodic obstacle arrays, *Phys. Rev. E* **95**, 030902(R) (2017).
- [22] H. Péter, A. Libál, C. Reichhardt, and C. O. Reichhardt, Crossover from jamming to clogging behaviours in heterogeneous environments, *Sci. Rep.* **8**, 10252 (2018).
- [23] C. Reichhardt and C. J. O. Reichhardt, Controlled fluidization, mobility, and clogging in obstacle arrays using periodic perturbations, *Phys. Rev. Lett.* **121**, 068001 (2018).
- [24] R. L. Stoop and P. Tierno, Clogging and jamming of colloidal monolayers driven across disordered landscapes, *Commun. Phys.* **1**, 68 (2018).
- [25] S. G. Leyva, R. L. Stoop, P. Tierno, and I. Pagonabarraga, Dynamics and clogging of colloidal monolayers magnetically driven through a heterogeneous landscape, *Soft Matter* **16**, 6985 (2020).
- [26] S. G. Leyva and I. Pagonabarraga, Clogging transition and anomalous transport in driven suspensions in a disordered medium, *Phys. Rev. E* **109**, 014618 (2024).
- [27] C. Reichhardt and C. J. O. Reichhardt, Directional clogging and phase separation for disk flow through periodic and diluted obstacle arrays, *Soft Matter* **17**, 1548 (2021).
- [28] G. Wang, L. Shen, J. Zhao, H. Liang, D. Xie, Z. Tian, and C. Wang, Design and compressive behavior of controllable irregular porous scaffolds: Based on Voronoi-Tessellation and for additive manufacturing, *ACS Biomater. Sci. Eng.* **4**, 719 (2018).
- [29] A. Mishra, P. Singh, and L. Li, Heat transfer model for moving packed-bed particle-to-sCO<sub>2</sub> heat exchangers integrated with metal foams, *Appl. Therm. Eng.* **239**, 122062 (2024).
- [30] K. J. Albrecht and C. K. Ho, Heat transfer models of moving packed-bed particle-to-sCO<sub>2</sub> heat exchangers, *J. Sol. Energy Eng.* **141**, 031006 (2019).
- [31] K. Randhir, M. Hayes, P. Schimmels, J. Petrasch, and J. Klausner, Zero carbon solid-state rechargeable redox fuel for long duration and seasonal storage, *Joule* **6**, 2513 (2022).
- [32] T. van de Laar, S. ten Klooster, K. Schroën, and J. Sprakel, Transition-state theory predicts clogging at the microscale, *Sci. Rep.* **6**, 28450 (2016).
- [33] T. Barker, C. Zhu, and J. Sun, Exact solutions for steady granular flow in vertical chutes and pipes, *J. Fluid Mech.* **930**, A21 (2022).
- [34] W. R. Ketterhagen, J. S. Curtis, C. R. Wassgren, and B. C. Hancock, Modeling granular segregation in flow from quasi-three-dimensional, wedge-shaped hoppers, *Powd. Technol.* **179**, 126 (2008).
- [35] A. Anand, J. S. Curtis, C. R. Wassgren, B. C. Hancock, and W. R. Ketterhagen, Predicting discharge dynamics of wet cohesive particles from a rectangular hopper using the discrete element method (DEM), *Chem. Eng. Sci.* **64**, 5268 (2009).
- [36] R. Artoni and P. Richard, Effective wall friction in wall-bounded 3D dense granular flows, *Phys. Rev. Lett.* **115**, 158001 (2015).
- [37] C. S. Campbell, Granular material flows—an overview, *Powder Technol.* **162**, 208 (2006).
- [38] H. Lu, J. Zhong, G.-P. Cao, and H.-F. Liu, Gravitational discharge of fine dry powders with asperities from a conical hopper, *AIChE J.* **64**, 427 (2018).
- [39] M. Souzy, I. Zuriguel, and A. Marin, Transition from clogging to continuous flow in constricted particle suspensions, *Phys. Rev. E* **101**, 060901(R) (2020).
- [40] R. Caitano, B. V. Guerrero, R. E. R. González, I. Zuriguel, and A. Garcimartín, Characterization of the clogging transition in vibrated granular media, *Phys. Rev. Lett.* **127**, 148002 (2021).
- [41] A. Janda, I. Zuriguel, A. Garcimartín, L. A. Pugnaloni, and D. Maza, Jamming and critical outlet size in the discharge of a two-dimensional silo, *Europhys. Lett.* **84**, 44002 (2008).
- [42] I. Zuriguel, A. Janda, A. Garcimartín, C. Lozano, R. Arévalo, and D. Maza, Silo clogging reduction by the presence of an obstacle, *Phys. Rev. Lett.* **107**, 278001 (2011).

- [43] A. B. Harada, E. Thackray, and K. N. Nordstrom, Silo flow and clogging in the presence of an obstacle, *Phys. Rev. Fluids* **7**, 054301 (2022).
- [44] K. A. Reddy, J. Talbot, and V. Kumaran, Dynamics of sheared inelastic dumbbells, *J. Fluid Mech.* **660**, 475 (2010).
- [45] S. Kumar, M. Dhiman, and K. A. Reddy, Magnus effect in granular media, *Phys. Rev. E* **99**, 012902 (2019).
- [46] A. V. K. Reddy, S. Kumar, and K. A. Reddy, Granular particle-shape heterogeneous mixtures discharging through a silo, *J. Fluid Mech.* **912**, A22 (2021).
- [47] L. Mullen, R. C. Stamp, W. K. Brooks, E. Jones, and C. J. Sutcliffe, Selective laser melting: A regular unit cell approach for the manufacture of porous, titanium, bone in-growth constructs, suitable for orthopedic applications, *J. Biomed. Mater. Res. Part B* **89B**, 325 (2009).
- [48] Y. Liu, X. Li, L. C. Zhang, and T. Sercombe, Processing and properties of topologically optimised biomedical Ti-24Nb-4Zr-8Sn scaffolds manufactured by selective laser melting, *Mater. Sci. Eng. A* **642**, 268 (2015).
- [49] S. C. Kapfer, S. T. Hyde, K. Mecke, C. H. Arns, and G. E. Schröder-Turk, Minimal surface scaffold designs for tissue engineering, *Biomaterials* **32**, 6875 (2011).
- [50] Z. Gorgin Karaji, M. Speirs, S. Dadbakhsh, J.-P. Kruth, H. Weinans, A. Zadpoor, and S. A. Yavari, Additively manufactured and surface biofunctionalized porous nitinol, *ACS Appl. Mater. Interfaces* **9**, 1293 (2017).
- [51] Z. Zhao, J. Li, D. Yao, and Y. Wei, Mechanical and permeability properties of porous scaffolds developed by a Voronoi Tessellation for bone tissue engineering, *J. Mater. Chem. B* **10**, 9699 (2022).
- [52] H. Hertz, On the contact of elastic solids, *J. Reine Angew. Math.* **1882**, 156 (1882).
- [53] Y. Tsuji, T. Tanaka, and T. Ishida, Lagrangian numerical simulation of plug flow of cohesionless particles in a horizontal pipe, *Powder Technol.* **71**, 239 (1992).
- [54] R. D. Mindlin, Compliance of elastic bodies in contact, *J. Appl. Mech.* **16**, 259 (1949).
- [55] R. D. Mindlin and H. Deresiewicz, Elastic spheres in contact under varying oblique forces, *J. Appl. Mech.* **20**, 327 (1953).
- [56] P. A. Cundall and O. D. Strack, A discrete numerical model for granular assemblies, *Géotechnique* **29**, 47 (1979).
- [57] H. Sakaguchi, E. Ozaki, and T. Igarashi, Plugging of the flow of granular materials during the discharge from a silo, *Int. J. Mod. Phys. B* **07**, 1949 (1993).
- [58] S. Chen, W. Fang, and S. Shi, Flow characteristics and packing structures of dense granular flow around an immersed cylindrical tube, *Chem. Eng. Sci.* **258**, 117773 (2022).
- [59] P. Bartsch and S. Zunft, Granular flow around the horizontal tubes of a particle heat exchanger: DEM-simulation and experimental validation, *Sol. Energy* **182**, 48 (2019).